Studies of equation of state properties of high-energy-density matter generated by intense ion beams at the facility for antiprotons and ion research

N. A. Tahir,[1] P. Neumayer,[1] I. V. Lomonosov,[2] A. Shutov,[3] V. Bagnoud,[1] A. R. Piriz,[4] S. A. Piriz,[4] and C. Deutsch[5]

[1]*GSI Helmholtzzentrum für Schwerionenforschung, 64291 Darmstadt, Germany*

[2]*Institute of Problems of Chemical Physics, Russian Academy of Sciences, 142432 Chernogolovka, Russia and Lomonosov Moscow State University, GSP-1, Leninskie Gory, 119991 Moscow, Russia and Moscow Institute of Physics and Technology, 141701 Dolgoprudny, Russia*

[3]*Institute of Problems of Chemical Physics, Russian Academy of Sciences, 142432 Chernogolovka, Russia*

[4]*E.S.T.I. Industriales, Universidad de Castilla-La Mancha, 13071 Ciudad Real, Spain*

[5]*Laboratoire de Physique des Gaz et des Plasmas, Universite Paris-Sud, 91405 Orsay, France*

(Received 27 May 2019; revised manuscript received 3 December 2019; accepted 10 January 2020; published 6 February 2020)

The work presented in this paper shows with the help of two-dimensional hydrodynamic simulations that intense heavy-ion beams are a very efficient tool to induce high energy density (HED) states in solid matter. These simulations have been carried out using a computer code BIG2 that is based on a Godunov-type numerical algorithm. This code includes ion beam energy deposition using the cold stopping model, which is a valid approximation for the temperature range accessed in these simulations. Different phases of matter achieved due to the beam heating are treated using a semiempirical equation-of-state (EOS) model. To take care of the solid material properties, the Prandl-Reuss model is used. The high specific power deposited by the projectile particles in the target leads to phase transitions on a timescale of the order of tens of nanosecond, which means that the sample material achieves thermodynamic equilibrium during the heating process. In these calculations we use Pb as the sample material that is irradiated by an intense uranium beam. The beam parameters including particle energy, focal spot size, bunch length, and bunch intensity are considered to be the same as the design parameters of the ion beam to be generated by the SIS100 heavy-ion synchrotron at the Facility for Antiprotons and Ion Research (FAIR), at Darmstadt. The purpose of this work is to propose experiments to measure the EOS properties of HED matter including studies of the processes of phase transitions at the FAIR facility. Our simulations have shown that depending on the specific energy deposition, solid lead will undergo phase transitions leading to an expanded hot liquid state, two-phase liquid-gas state, or the critical parameter regime. In a similar manner, other materials can be studied in such experiments, which will be a very useful addition to the knowledge in this important field of research.

DOI: 10.1103/PhysRevE.101.023202

I. INTRODUCTION

States of matter which correspond to an energy content of 10^{11} J/m^3, or, equivalently, 1 Mbar pressure, are classified as high-energy-density (HED) states [1,2]. The importance of HED physics is underscored by the fact that it spans over very wide areas of basic and applied research including, for example, astrophysics [3,4], planetary physics [5–8], inertial fusion [9–11], strongly coupled plasmas [12–14], and many others. An accurate knowledge of the thermophysical and the transport properties of HED matter is therefore crucial to our understanding of these very important areas of physics. Over the past decades, extensive experimental work has been done in this field using static as well as dynamic techniques. The most commonly used static configuration employs a diamond anvil cell (DAC), in which the sample material is subjected to ultrahigh static pressures, thereby generating extreme physical conditions in the material [15,16]. The traditional dynamic techniques, on the other hand, involve shock compression of matter. Due to the shock, the material is compressed and irreversibly heated, leading to high values of pressure and entropy in the sample material. These shocks are generated using high-power chemical explosives, light gas guns, Z-pinches, powerful lasers, and nuclear explosions [17–28].

Recent developments in the technology of well-focused, strongly bunched intense beams of energetic particles have provided the scientists with an additional very efficient and flexible tool to study HED physics in the laboratory. A new international accelerator project named Facility for Antiprotons and Ion Research (FAIR) entered into the construction phase in July 2017 in Darmstadt, Germany [29–32]. The main accelerator that is being built at this facility is a heavy-ion synchrotron, named SIS100. It is expected that SIS100 will be commissioned in the year 2025. A wide-range physics research program has been prepared for this facility and HED physics research is an important part of this program [33–51]. Another important problem that will be studied at this facility is the production of radioactive beams [52–54]. It is also worth mentioning that due to the high efficiency and high repetition rate of the accelerator and favorable ion energy deposition in the target, heavy ions are considered as a viable driver for any future inertial fusion reactor system [55–66].

In this paper we discuss the overall potential of the FAIR facility to study HED physics and present a specific

experiment design that will be used to investigate the equation-of-state (EOS) properties of HED matter. It is also important to note that the proton beams generated by another powerful accelerator, the Large Hadron Collider (LHC), has the potential to generate HED matter [67,68].

In Sec. II we discuss the potential of the FAIR ion beam to do HED physics research, while in Sec. III, we describe an experimental scheme named heavy ion heating and expansion (HIHEX) that can be used to study the EOS properties of HED matter. Section IV presents the beam parameters and the target design, whereas the BIG2 computer code is described in Sec. V. Numerical simulation results are given in Sec. VI and the diagnostics are discussed in Sec. VII. The conclusions drawn from this work are noted in Sec. VIII.

II. FACILITY FOR ANTIPROTONS AND ION RESEARCH AND HIGH-ENERGY-DENSITY PHYSICS

The main accelerator at the FAIR facility, SIS100, is a heavy-ion synchrotron with 100-Tm magnetic rigidity. The SIS100 is designed to deliver intense beams of energetic ions of all stable species from proton up to uranium. Slow as well as fast extraction options will be available. In the former scheme a continuous beam is generated, while in the latter case, a bunched beam is produced. Use of a powerful bunch compressor will provide a single short bunch of duration 70–100 ns in the fast extraction case. An advanced focusing system will focus the beam to a spot size of the order of 1-mm radius. The maximum beam intensity is expected to be 5×10^{11} uranium ions/bunch.

Beam-matter interaction has been a subject of interest over the past many decades. Extensive theoretical and experimental work has been done in this area, but so far the interest has been limited to studying the interaction of individual particles with the target material. The main purpose of these works was, for example, to calculate or measure the projectile energy loss in matter [69–71] or to study the damage caused to the material by the impact of the incident particles [72–74]. In these cases, the overall temperature and hence the phase state of the material is not affected because the total energy deposited in the target is negligible due to the low beam intensity. However, with the availability of high -intensity particle beams, the nature of beam-matter interaction is totally changed. The high-intensity beam deposits huge specific energy in a small volume that generates high temperatures, which lead to phase transitions. Moreover, high temperatures produce high pressures, which generate shock waves that compress and heat the material. An intense ion beam therefore has the potential to be a viable driver for generating HED matter in the laboratory.

Extensive theoretical work has been done during the past two decades to assess the feasibility of the SIS100 beam to do HED physics research at FAIR [34–51]. This work has shown that the ion beam can be employed to generate HED matter using two very different experimental configurations. In one scheme, a HED sample is generated using isochoric and uniform heating of a solid target [34,36,37], while in the other, shock compression is considered to achieve this goal [37,39,41,42]. It is to be noted that such flexibility is not offered by any other driver, which underscores the importance of an ion beam driver. In these studies a uranium beam is considered because it provides the maximum specific energy deposition due to its highest charge.

It is also worth noting that recent developments in the field of high-intensity petawatt lasers has lead to generation of intense, collimated ultrashort-pulse proton beams [75–80]. It has been shown [81,82] that these beams can be used for isochoric heating of matter in a similar manner using heavy-ion beams as mentioned above. However, there are a number of advantages in using heavy-ion beams compared to the laser-generated proton beams, as briefly discussed below.

One of the key requirements in studying the EOS of HED matter using isochoric heating by particles is uniformity of physical conditions in the sample material. Moreover, the size of the sample should be large enough to facilitate the diagnostics. The transverse particle intensity distribution in case of accelerator delivered heavy-ion beams as well as the laser-generated proton beams is approximately Gaussian. In order to achieve uniform energy deposition in the target in the transverse direction, the target dimensions should be less than the full width at half maximum (FWHM) of the Gaussian intensity distribution. In case of the heavy ions, for example with the SIS100 beam, one can have a spot size with a FWHM of 1–3 mm that will induce sufficient specific energy in the target material. One therefore can use a target with a thickness (diameter) of 200–500 μm. In case of currently available laser-generated proton beams, one can have a beam FWHM of the order of 50 μm that would restrict the target size to a thickness (diameter) of the order of 10 μm.

In order to achieve uniform energy deposition along the longitudinal direction, the ion range should be large compared to the target length so that the Bragg peak does not lie inside the sample. In case of accelerator produced heavy ions, one has great flexibility in choosing the particle energy so that one can take a high energy that will provide a large particle range in the sample material and the target could be up to a few mm long. In case of laser-generated protons, on the other hand, one has little control on the particle energy as it is primarily determined by the laser intensity and energy, which restricts the sample dimensions. Furthermore, accelerators are capable of generating monoenergetic ions, whereas in case of laser-generated protons, the energy spread is of the order of 100%, which may lead to nonuniform energy deposition. Another problem that one may face in using highly collimated proton beams and very thin target is the proper target alignment with respect to the beam.

To oversee the construction of the experimental facilities and later carry out the experiments included in the HED physics scientific proposal, an international collaboration that includes around 100 scientists from 10 countries, named HED@FAIR, has been organized. Details of one of the proposed experiments are presented in this paper.

III. HEAVY ION HEATING AND EXPANSION SCHEME

As discussed in the previous section, an intense beam of energetic ions delivered by an accelerator can efficiently heat solid targets isochorically and uniformly. This unique feature of an ion beam driver is exploited in the proposed HIHEX scheme. The heated material is subsequently allowed

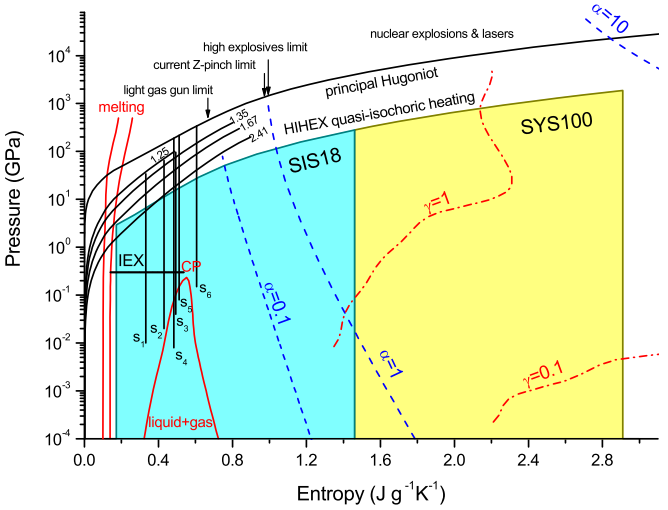

FIG. 1. Pressure-entropy phase diagram for lead. All the experimentally studied regions using different techniques are plotted. The principal and porous Hugoniots investigated in shock wave compression experiments (the numbers near Hugoniot curves indicate porosity, $V_{\text{porous}}/V_{\text{solid}}$), the only-studied release isentropes (S_1 to S_6) from Refs. [17,20–22], and isobaric expansion (IEX) [83] are shown along with the parameter space which will be accessible with HIHEX technique. Possibilities of shock wave drivers are also plotted using the data from Refs. [17,20–22] for light-gas guns, high explosive generators, and Z-pinch [23]. The physical characteristics such as melting and evaporation curves, the critical point, isolines of ionization degree (α), and nonideality parameter (γ) [84] are also shown.

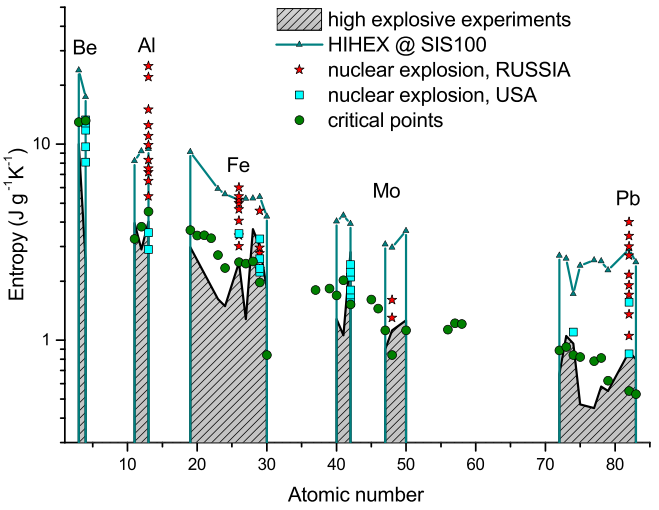

FIG. 2. Entropy vs atomic number showing the high-entropy states obtained by different experimental methods for different metals including those which can be accessed by the HIHEX technique using the SIS100 uranium beam.

to expand isentropically that ends up in one of the HED states. For example, an expanded hot liquid state, two-phase liquid-gas state, critical point parameters and a strongly coupled plasma state. The final state that the sample material will achieve in an experiment depends on the level of the specific energy deposition.

Figure 1 shows an entropy-pressure phase diagram of lead. It is seen that the data achieved by shock compression is limited to the region of the principal Hugoniot. There are four porous Hugoniot curves and six release isentropes. Some of the release isentropes end up in expanded hot liquid state, some in the two-phase liquid-gas region and one passes through the critical point region. Moreover, the critical point region can also be accessed using the IEX (exploding wire) technique. However, the rest of the phase diagram that includes the interesting region of strongly coupled plasmas has never been accessed using the existing methods. It is to be noted that lead is one of the few well-studied materials, while for majority of the metals, little experimental data are available. The solid curve below the principal Hugoniot is the thermodynamic path that the material will follow in a HIHEX experiment. One may achieve a specific point on this path by depositing the corresponding amount of specific energy in the sample material. The required HED state below this curve can then be accessed by allowing the heated material to expand isentropically. It is seen that the SIS100-generated uranium beam is powerful enough to access the entire phase diagram using the HIHEX technique.

In Fig. 2 we show the high-entropy states for various metals that can be achieved using the HIHEX method compared to other existing techniques. We used the available data obtained in shock compression experiments performed with high explosives and underground nuclear explosions to calculate these entropy states. Evaluated critical points [85–87] indicating the typical entropy region of strongly coupled plasmas are also shown in Fig. 2 and in Table I. Estimated regions of isochoric heating in the future HIHEX experiments using SIS100 at FAIR are plotted as well. It is seen that level of entropy induced by the HIHEX scheme using the SIS100 beam is comparable to that generated by nuclear explosions.

In Table I we present estimated critical parameters for some of the metals. It is seen that the critical temperature for a number of metals is very high, which is very difficult to access by the shock wave technique. However, this does not seem to pose any problem in the proposed HIHEX scheme. It is thus expected that these experiments will generate wealth of new information in this area of research.

TABLE I. Critical point parameters of some metals.

	T_c (K)	P_c (kbar)	ρ_c (g/cm^3)
Lead	5500	2.30	3.10
Gold	8500	6.14	6.10
Zinc	3080	3.30	2.40
Copper	7800	9.00	2.28
Silver	7050	10.64	3.28
Beryllium	8877	2.872	0.398
Iridium	11640	6.20	3.10
Tin	8175	2.39	1.592
Uranium	9637	7.70	4.505
Aluminum	6250	1.97	0.703
Tungsten	15750	11.80	4.854
Niobium	19200	11.10	1.70
Tantalum	13530	9.93	4.263

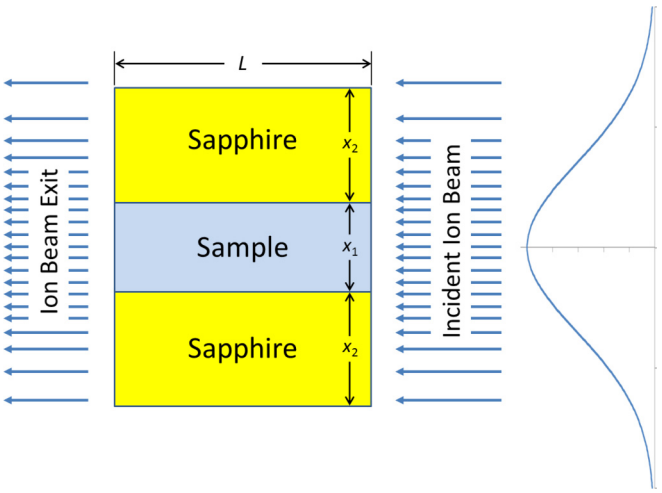

FIG. 3. Proposed beam-target geometry using plane HIHEX scheme.

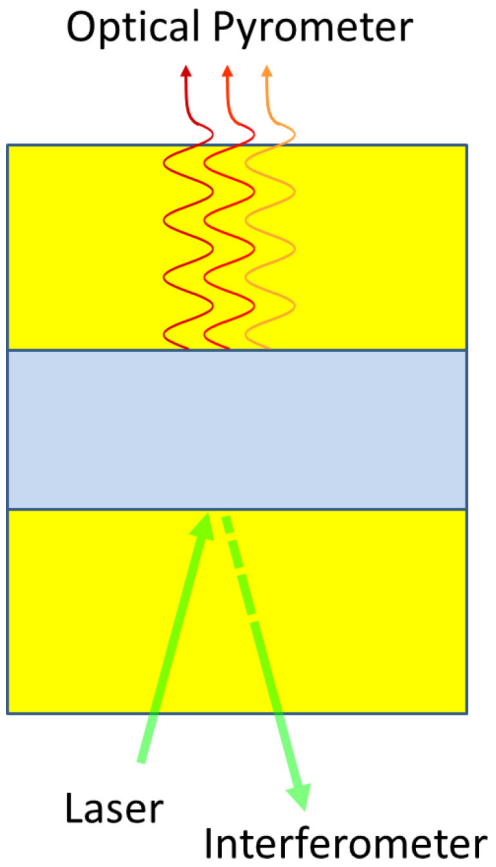

FIG. 4. Optical diagnostic scheme.

IV. BEAM PARAMETERS AND TARGET DESIGN

Figure 3 shows the schematics of a HIHEX experimental configuration using plane geometry. The sample is a thin plate that is sandwiched between two sapphire slabs. The sapphire slabs act as an optical window with a transmission range of 0.17–5.5 μm, which includes infrared to ultraviolet region of the spectrum. Sapphire is a mechanically strong material with a yield strength of 345 MPa at a temperature of 1000 K. Moreover, it has a density of 3.98 g/cm^3 and a melting temperature of 2303 K. It can withstand high pressures and thermal shocks, while maintaining its transparency and structural stability [88]. These characteristics make sapphire an attractive material for constructing an optical window. In addition to that, the sapphire blocks act as a tamper that confines the sample material for a longer time.

The beam is incident transversely on one side of the target, as shown in Fig. 3. The particle energy is high enough to make the ion range larger than the target length. This ensures uniform energy deposition along the particle trajectory as the Bragg peak lies outside the target. Moreover, the transverse intensity distribution in the focal spot is a Gaussian. The FWHM of the focal spot and the thickness of the sample are arranged in such a way that most of the ions deposit their energy in the sample, while the sapphire plates are irradiated only by the the wings of the Gaussian distribution. As a result, the sample is converted into HED matter, while the sapphire remains solid that will allow the use of optical diagnostics (see Fig. 4).

Due to the strong heating by the beam, the sample is converted into HED matter that expands due to the high pressure. The sapphire plates are symmetrically pushed outward and the density of the sample material is reduced uniformly along the width. Depending on the level of the deposited specific energy, a given HED state can be generated.

V. COMPUTER CODE BIG2

The BIG2 is a two-dimensional hydrodynamic computer code that is based on a Godunov-type numerical algorithm, which uses a finite-volume approach in the space-time domain. The fluxes are calculated using the solution of Riemann problem at each intercell boundary [89]. It is a conservative scheme that has a second-order accuracy in space and first-order accuracy in time. The code is based on a Eulerian numerical scheme that uses curvilinear rectangular moving grid. The grid is adaptive to gradient of physical parameters (pressure, temperature, and density) due to the condensation of the grid lines. The movement of the grid boundary is calculated in accordance with the type of the boundary, for example, it could be a shock front, a material interface, a free boundary, a rigid wall, and so on. Reconstruction of the grid at the new time step is carried out by quasiconformal mapping of the rectangular grid to the area with the numerical grid boundary calculated at the new time step, taking into account the gradient of the specified physical parameter. Further details about the numerical techniques used in the code can be found in Ref. [90]. The BIG2 code can treat multilayered targets composed of different materials and can handle complicated target geometries.

The ion beam energy deposition in the material is calculated assuming a cold stopping model described in Ref. [70]. This is a valid approximation because in ion-beam heated targets, the temperature is rather low (below 10 eV) so that the ionization effects are negligible. The plasma effects on the stopping power become important when the ionization level in the material is significant, which requires a much higher temperature.

Due to the beam heating, the target material passes through different material phases, which are treated using a semiempirical EOS model described in Refs. [91,92]. This model considers macroscopically correct equation of state that accounts for solid, liquid, and gaseous states as well as the melting and the evaporating two-phase regions. On our timescales (around 100 ns), we consider the target material is under conditions of the local thermodynamic equilibrium. So we apply in numerical modeling of expanded target the equation of state in tabular form, using Maxwell construction in the two-phase liquid-gas region, as it has been discussed in Ref. [93].

To simulate the mechanical (elastic-plastic) properties of solid materials, we use the nonlinear Prandtl-Reuss model with the von Mises yield criterion, which is given by the following differential equations for the deviatoric part S_{ik} of the stress tensor $\sigma_{ik} = -P\,\delta_{ij} + S_{ik}$ (where P is the pressure, and δ_{ik} is the Kronecker tensor) [94]:

$$\dot{S}_{ik} = 2GD_{ik} \tag{1}$$

if $S_{ik}D_{ik} < 0$ or $S_{ik}S_{ik} < \frac{2}{3}Y^2$

$$\dot{S}_{ik} + 2GS_{ik}\frac{S_{mn}D_{mn}}{S_{mn}S_{mn}} = 2GD_{ik} \tag{2}$$

if $S_{ik}D_{ik} > 0$ and $S_{ik}S_{ik} = \frac{2}{3}Y^2$.

Here G is the shear modulus, Y is the yield strength, and both are parameters characteristic of the solid material, which to the scope of a parametric study are taken as independent and constant parameters. Besides, in Eqs. (1) and (2), D_{ik} is the strain rate tensor:

$$D_{ik} = \frac{1}{2}\left(\frac{\partial v_i}{\partial x_k} + \frac{\partial v_k}{\partial x_i} - \frac{2}{3}\frac{\partial v_j}{\partial x_j}\delta_{ik}\right). \tag{3}$$

VI. SIMULATION RESULTS

The numerical simulation results of the thermodynamic and the hydrodynamic response of the target shown in Fig. 3, are presented in this section. These simulations have been carried out employing a two-dimensional hydrodynamic computer code, BIG2, which is described in Sec. V and in Ref. [90].

The sample used in the present case, is a solid lead plate that is surrounded by a sapphire block, on each side. The target is irradiated with a single bunch composed of 1 GeV/u uranium ions having a bunch length of 100 ns. Different values of the beam intensity, including 3×10^{10}, 5×10^{10}, 7.5×10^{10}, and 10^{11} ions per bunch, respectively, are considered. Various focal spot sizes characterized with FWHM, including 1, 1.5, 2, 2.5, 3, and 3.5 mm, respectively, are used.

A. Bunch intensity 3×10^{10}

First, we discuss the simulation results obtained using the lowest beam intensity, 3×10^{10} ions per bunch. The focal spot size is characterized with FWHM = 2 mm considering a Gaussian transverse intensity distribution in the focal spot. Figure 5 shows the initial target geometry and the density distribution provided by the BIG2 code. The target length is 4 mm, whereas the thickness of the sample and the sapphire plates are 200 and 300 μm, respectively. Due to the ion energy deposition, the sample is strongly heated that generates

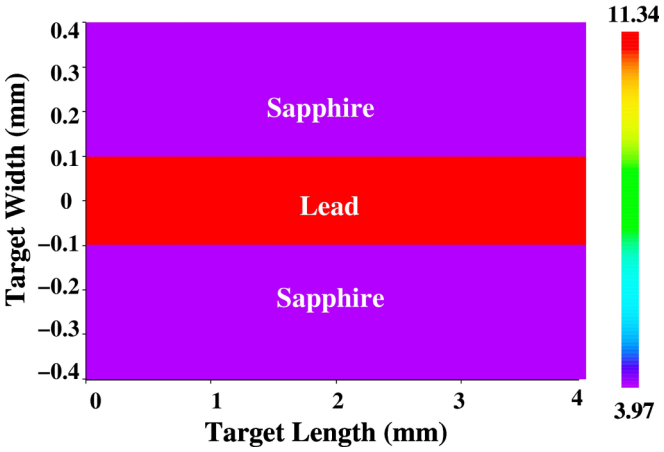

FIG. 5. Initial target density distribution provided by the BIG2 hydrodynamic code.

high temperature, which leads to high pressure. As a result, the sample material is converted into HED matter. In Fig. 6, we present the target physical conditions on a length-thickness plane at $t = 100$ ns, when the bunch has just delivered its total energy. Figure 6(a) presents the specific energy deposition distribution in the target. It is seen that the energy is uniformly deposited in the target in the longitudinal as well as in the transverse direction. The average specific energy deposition in the lead region is about 1 kJ/g, while in the sapphire, it has a higher value of 1.5 kJ/g.

Figure 6(b) shows that the average temperature in the lead sample is of the order of 6800 K, whereas in sapphire it has a much lower value of 1690 K, which is safely below the melting temperature. This means that the sapphire will remain solid, which will make it possible to diagnose the HED lead sample using the optical diagnostics discussed in Sec. VII.

The corresponding pressure and the density distributions are presented in Figs. 6(c) and 6(d), respectively. It is seen in Fig. 6(c) that a high pressure of about 9.5 GPa is generated in the lead, while Fig. 6(d) shows that the density is still close to the solid density. The material phase state is presented in Fig. 6(e), which indicates that the lead is converted into a hot liquid, whereas the sapphire remains solid.

In Fig. 7, we present the target physical conditions at $t =$ 240 ns. Figure 7(a) shows a substantial temperature reduction in the lead, whereas in the sapphire region, it does not show any significant change. This is due to the expansion of the liquefied lead caused by the high pressure, while the sapphire remains solid. The solid sapphire plates are symmetrically pushed in the opposite direction and they maintain their temperature. It is also seen that there is slight lateral expansion of the lead as well.

The corresponding pressure distribution is presented in Fig. 7(b). This pressure distribution is rather complicated due to the multiple reflection of the sound waves between the solid sapphire plates. It is seen that the pressure has been reduced by about two orders of magnitude in the lead as compared to that at $t = 100$ ns.

The density distribution at $t = 240$ ns is presented in Fig. 7(c). It is seen that the lead density has been reduced to about 6 g/cm^3 and the lead thickness has been extended to

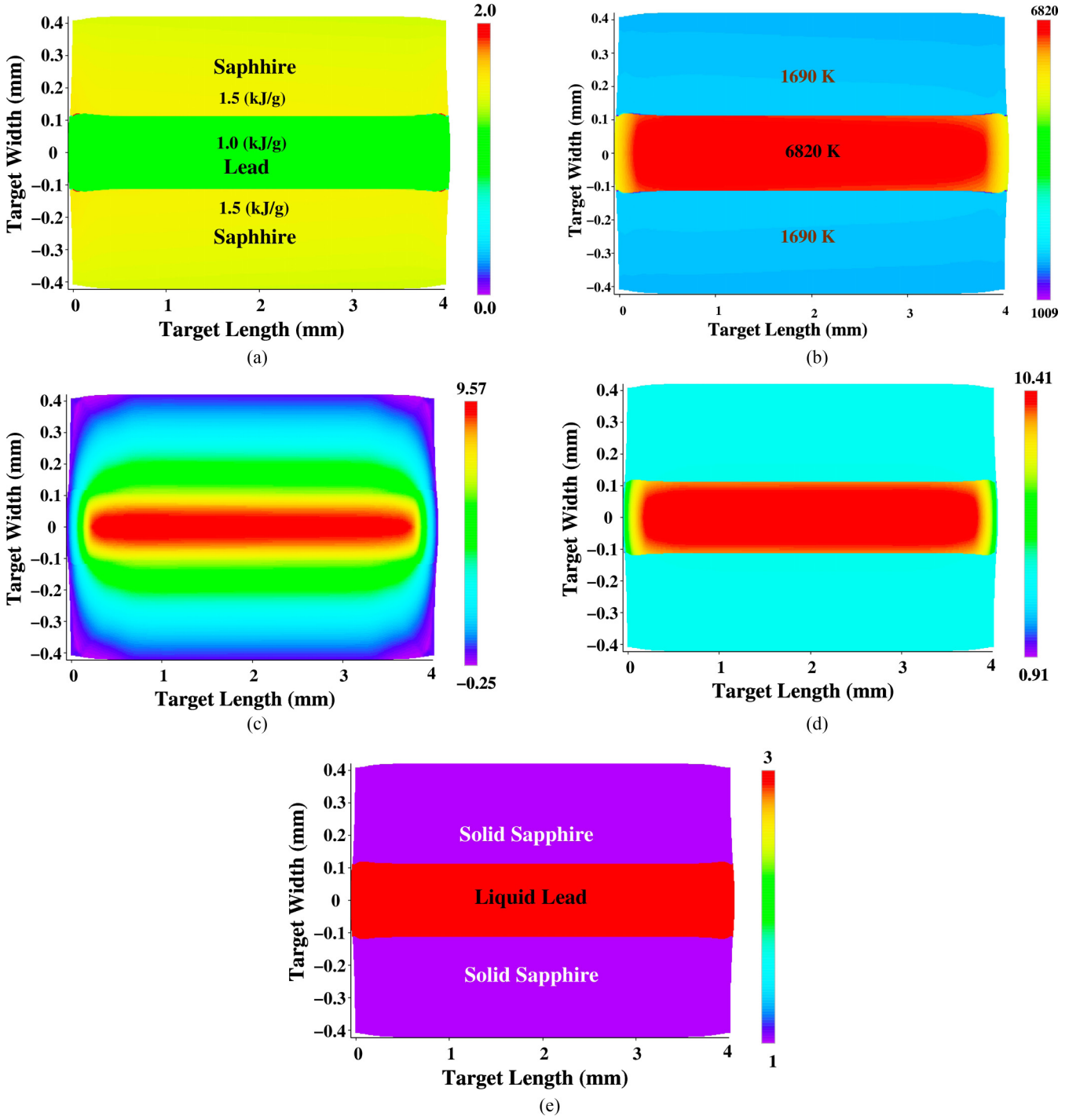

FIG. 6. Target physical conditions generated by BIG2 code at $t = 100$ ns, intensity $= 3 \times 10^{10}$ uranium ions per bunch, particle energy $=$ 1 GeV/u, bunch length $= 100$ ns, Gaussian transverse intensity distribution in focal spot with FWHM $= 2$ mm, target initial conditions as shown in Fig. 5; (a) specific energy distribution (kJ/g), (b) temperature distribution (K), (c) pressure distribution (GPa), (d) density distribution (g/cm^3), and (e) phase-state distribution.

400 μm. Moreover, some low-density lead is ejected in the lateral direction.

The corresponding material physical-state distribution is presented in Fig. 7(d). It is seen that the lead in most part of the target is in an expanded hot liquid state, whereas a small region at the boundaries has become a two-phase liquid-gas mixture.

Figures 6 and 7 show that the lateral material expansion is not significant over the considered timescale. The problem therefore is of quasi-one-dimensional expansion along the transverse coordinate, especially in the middle of the target. In such a case, it is a valid approximation to perform one-dimensional simulations along the target thickness. Moreover, one-dimensional profiles of density, temperature, and

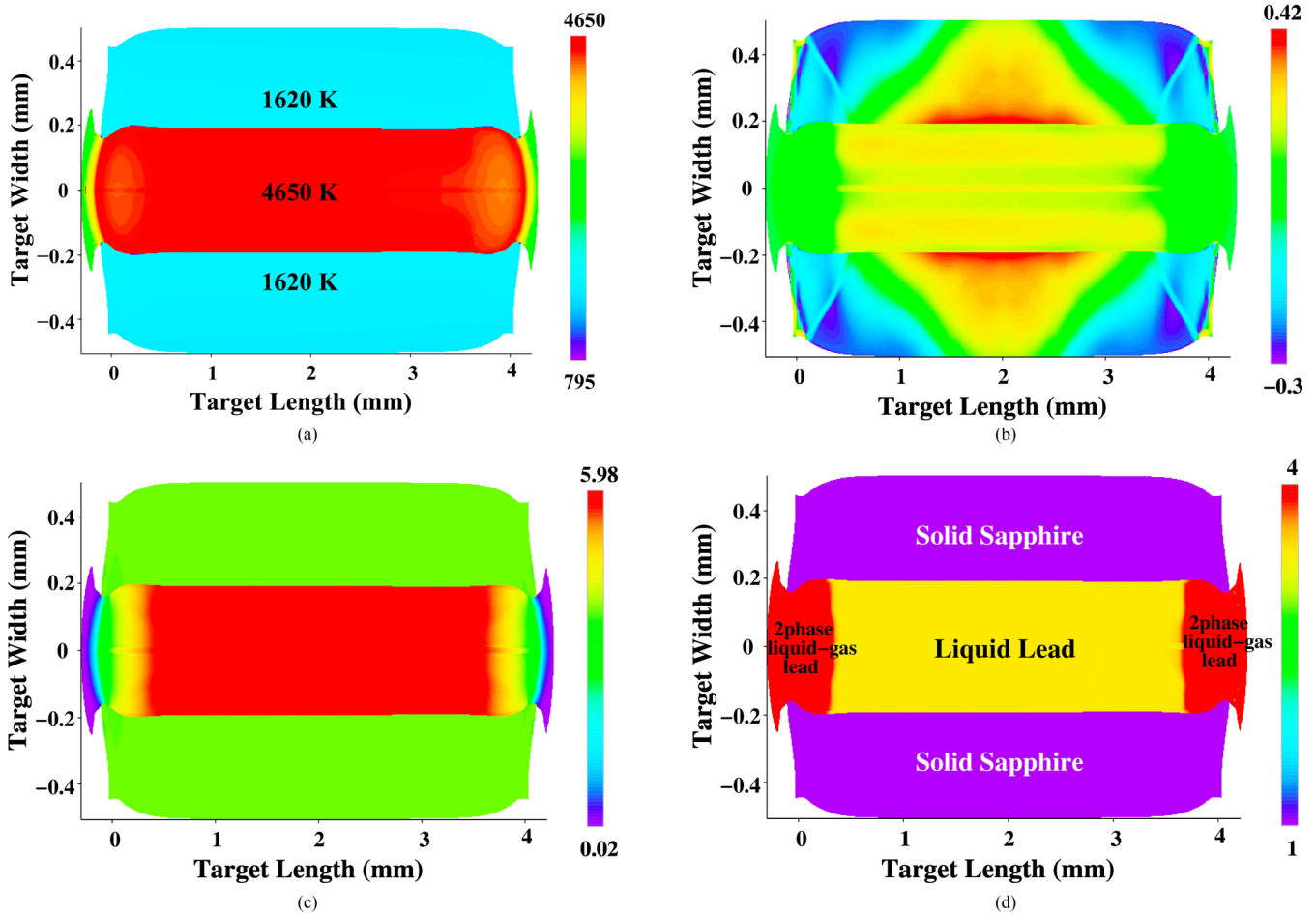

FIG. 7. Target physical conditions generated by BIG2 code at $t = 240$ ns, intensity $= 3 \times 10^{10}$ uranium ions per bunch, particle energy $=$ 1 GeV/u, bunch length $= 100$ ns, Gaussian transverse intensity distribution in focal spot with FWHM $= 2$ mm, target initial conditions as shown in Fig. 5; (a) temperature distribution (K), (b) pressure distribution (GPa), (c) density distribution (g/cm^3), and (d) physical-state distribution.

pressure provide more quantitative information about the material physical conditions during, and after the heating. This information is presented in the following.

1. One-dimensional profiles using FWHM of 2.5 mm

First, we present the results using a FWHM $= 2.5$ mm. Since the focal spot size is much larger than the target dimensions, the energy deposition is very uniform along the transverse direction. According to the simulations, a specific energy of about 0.65 kJ/g is deposited in the lead, while a higher value of around 1 kJ/g is achieved in the sapphire. In Fig. 8(a), we plot the density, temperature, and pressure vs the transverse coordinate at $t = 100$ ns, when the bunch has delivered its total energy. It is seen that the temperature in the lead sample is around 4600 K, while the pressure is about 70 kbar. The density is close to the solid density and the material is in the liquid state. It is also important to note that the temperature in the sapphire region is about 1100 K, which is significantly lower than the melting temperature. This means that the sapphire will remain solid and the heated sample can be successfully diagnosed through the sapphire window using optical diagnostics.

Figure 8(b) shows the same parameters as Fig. 8(a) but at $t = 200$ ns. It is seen that the lead has expanded in the transverse direction to a position of 150 μm from an initial position of 100 μm. The density has been reduced to about 8 g/cm^3, the temperature has decreased to around 3700 K, whereas the pressure is of the order of 10 kbar. The lead is now in an expanded hot liquid phase. The sapphire plates remain solid and are symmetrical pushed in the transverse direction due to the expansion of the lead.

Figure 8(c) is plotted at $t = 400$ ns, which shows that the lead has further expanded to a position of 225 μm. The lead density at this time is about 5 g/cm^3, the temperature is around 3300 K, and pressure is of the order of 0.06 kbar. These conditions represent a two-phase liquid-gas mixture of lead.

Figure 8(d) is plotted at $t = 600$ ns, which shows that the lead has further expanded to a transverse position of 300 μm, while the density has been reduced to 3.7 g/cm^3. The temperature and the pressure remain the same as in the previous figure.

Figure 8(e) shows the density, temperature, and pressure profiles at $t = 1000$ ns. It is seen that the lead has further expanded to a transverse position of 470 μm, while the density has been reduced to 2.4 g/cm^3.

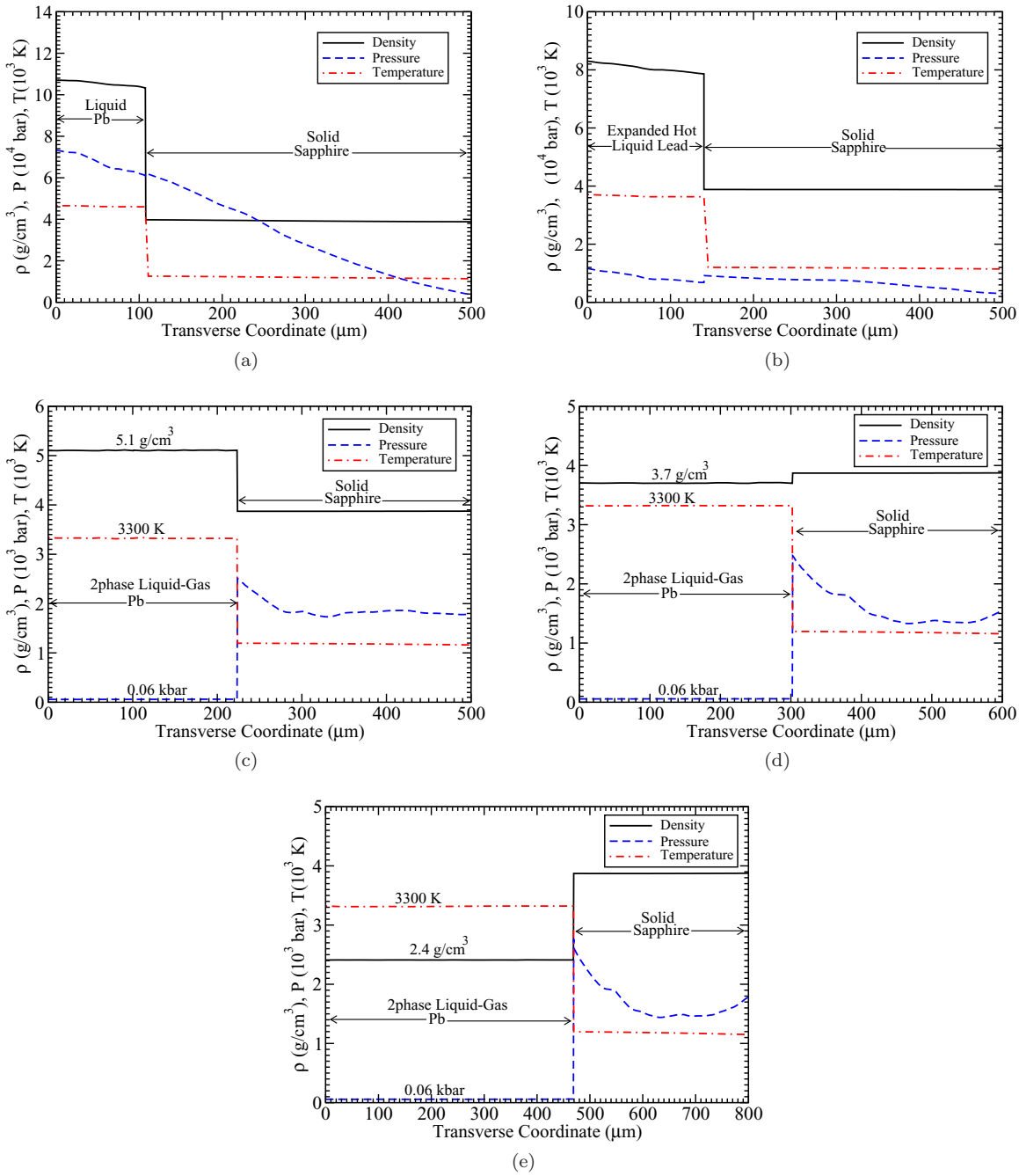

FIG. 8. Density (ρ), temperature (T), and pressure (P) vs transverse coordinate, intensity $= 3 \times 10^{10}$ uranium ions per bunch, particle energy $= 1$ GeV/u, bunch length $= 100$ ns, Gaussian transverse intensity distribution in focal spot with FWHM $= 2.5$ mm, target initial conditions as in Fig. 5; (a) at $t = 100$ ns, (b) at $t = 200$ ns, (c) at $t = 400$ ns, (d) at $t = 600$ ns, and (e) at $t = 1000$ ns.

These simulations indicate that using a low intensity of 3×10^{10} uranium ions per bunch and using a reasonable focal spot size, one may generate interesting HED states of lead, including an expanded hot liquid state and two-phase liquid-gas state. Moreover, one can generate a wide range of physical parameters that belong to the two-phase liquid-gas region of the sample material.

It is interesting to note that in Fig. 8(c), the thermal pressure in the lead is much lower than the thermal pressure in the sapphire. However, Figs. 8(d) and 8(e) show that the lead-sapphire boundary continues to move toward the right, in the direction of the positive pressure gradient, which may look unusual at the first glance. A more careful consideration shows that at $t = 100$ ns, the time when the bunch has just delivered its total energy to the target, the pressure in the Pb is much higher than in the sapphire and the boundary starts moving outward [see Fig. 8(a)]. Due to the heating by the beam, the Pb first melts and then starts to evaporate producing a two-phase liquid-gas mixture. The sapphire, on the other hand, remains solid with all the mechanical properties. The sapphire block

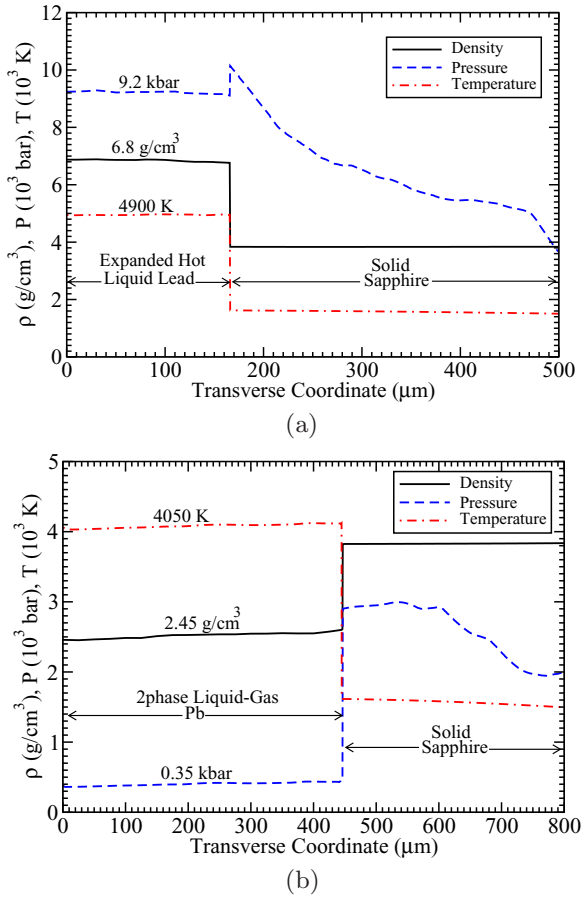

FIG. 9. Same as in Fig. 8 but using FWHM = 2 mm; (a) at t = 220 ns and (b) at t = 700 ns.

behaves as an almost-rigid body and continues moving due to its inertia, even after the pressure in the lead becomes lower than in the sapphire.

The interface Pb-sapphire is in equilibrium, and in this equilibrium of forces also participates the normal component S_{xx} (x is the transverse coordinate) of the deviatoric tensor S_{ik}. Since Pb is a gas [$S_{xx}^{(\mathrm{Pb})} = 0$], the equilibrium of forces $\sigma_{ik}^{(\mathrm{Pb})} = \sigma_{ik}^{(\mathrm{sapph})}$ at the Pb-sapphire interface reads: $P^{(\mathrm{Pb})} = P^{(\mathrm{sapph})} - S_{xx}^{(\mathrm{sapph})}$. Thus, the observed jump at the interface is just equal to $S_{xx}^{(\mathrm{sapph})}$, and pressure in Pb must be lower than the pressure in sapphire.

This behavior is observed in all the following simulation results.

2. One-dimensional profiles using FWHM of 2 mm

We now present simulation results using the same target and beam parameters as in the previous case but considering a somewhat more focused beam with spot size characterized with FWHM = 2 mm. Figure 9(a) shows density, temperature, and pressure vs the transverse coordinate at t = 220 ns. It is seen that the lead has expanded and the lead-sapphire boundary has moved to a position of 160 μm, while the density has been reduced to 6.8 g/cm^3. The temperature is about 4900 K, whereas the pressure is of the order of 9.2 kbar. These conditions represent the interesting phase of expanded hot liquid lead.

In Fig. 9(b), we plot the same physical parameters as in the previous one but at t = 700 ns. The lead density has been further reduced to 2.45 g/cm^3, while the temperature is about 4050 K and the pressure is around 0.35 kbar. These conditions represent two-phase liquid-gas state of lead. It is also important to note that the profiles in the lead are very uniform, which is very good for the accuracy of the experimental measurements.

It is also to be noted that the temperature in the sapphire is of the order of 1500 K, which means that the sapphire plates on either side of lead remain in solid phase. This will facilitate measurement of the sample physical parameters using optical diagnostics.

B. Bunch intensity 5 × 10^{10}

In this section we present the simulation results using a higher beam intensity of 5 × 10^{10} ions per bunch. Since the beam intensity is higher, if one uses a less focused beam with a larger focal spot, then the specific energy deposition will still be large enough to induce HED states in the sample. A wider focal spot leads to a more uniform energy deposition in the transverse direction and it also allows using a larger sample size. In the present calculations we use a 500-μm-thick lead sample, which means X_1 = 500 μm (see Fig. 3). Also the thickness of each sapphire plate is 500 (X_2 = 500 μm). We have considered different values of FWHM of the Gaussian transverse intensity distribution, including 3.5 mm, 3 mm, and 2 mm, respectively, and the results are presented below.

1. One-dimensional profiles using FWHM of 3.5 mm

First, we present results using the biggest value of FWHM of 3.5 mm. According to the simulations, a specific energy of 0.6 and 0.82 kJ/g is deposited in the lead and the sapphire, respectively. Figure 10(a) shows the density, temperature, and pressure vs the transverse coordinate at t = 425 ns. It is seen that the lead has expanded to a lower density of 7.5 g/cm^3, while the temperature and the pressure are 2940 K and 0.022 kbar, respectively. It is seen that the profiles are fairly uniform along the transverse coordinate and the sample is in two-phase liquid-gas state. The temperature in the sapphire is about 1000 K, which shows that the sapphire remains in solid state.

Figure 10(b) presents the same profiles as the previous figure but at a later time, t = 700 ns. The lead has further expanded to a lower density of 5.7 g/cm^3, while the sample remains in two-phase liquid-gas state. It is to be noted that the sapphire blocks are symmetrically moved outward as the lead expands. In this figure, we only show a part of the sapphire region.

Figure 10(c) shows the same variables as in the previous figure but at t = 1000 ns. It is seen that due to the further expansion in the transverse direction, the lead density has become 4.6 g/cm^3, while the temperature and the pressure remain constant. These physical conditions correspond to two-phase liquid-gas state of lead. It is also seen that the profiles presented in these figures are very uniform in the lead region.

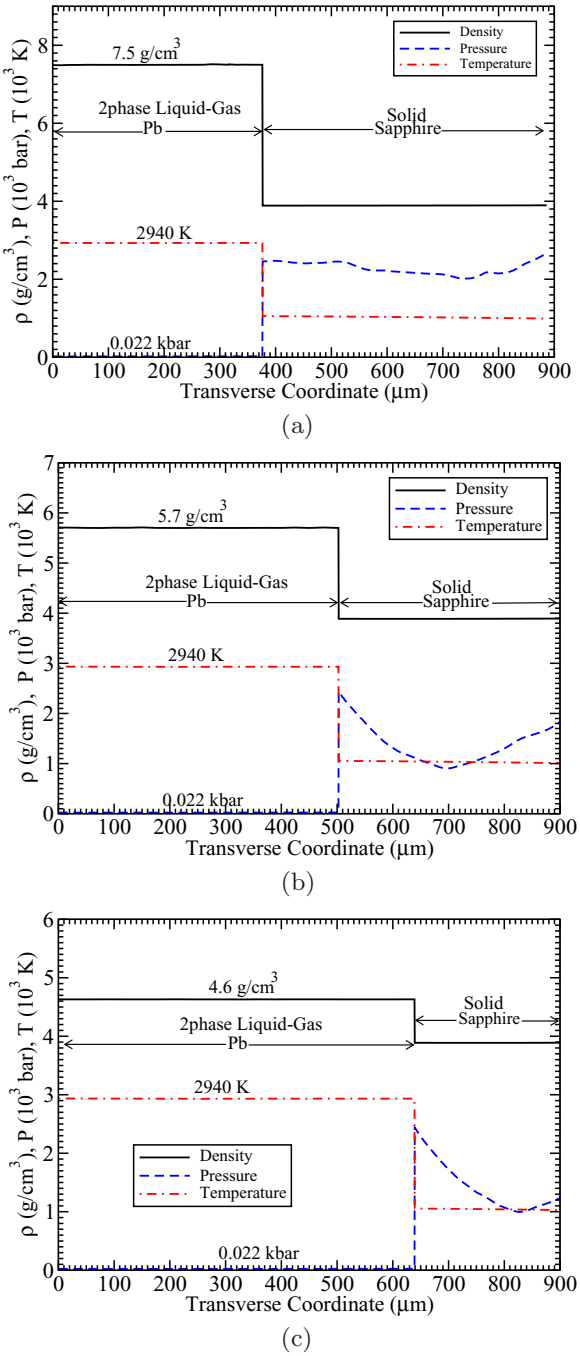

FIG. 10. Density (ρ), temperature (T), and pressure (P) vs transverse coordinate, intensity $= 5 \times 10^{10}$ uranium ions per bunch, particle energy $= 1$ GeV/u, bunch length $= 100$ ns, Gaussian transverse intensity distribution in focal spot with FWHM $= 3.5$ mm, sample thickness $= 500$ μm, sapphire thickness 500 μm (Fig. 3); (a) at $t = 425$ ns, (b) at $t = 700$ ns, and (c) at $t = 1000$ ns.

It is to be noted that as the bunch delivers its energy to the target, the lead is first converted into high-density liquid that expands and the density decreases and the sample becomes an expanded hot liquid. Further expansion leads to further reduction in density and temperature and the material enters two-phase liquid-gas region. We do not present the initial profiles representing the liquid phase but show selected examples of profiles in the two-phase state.

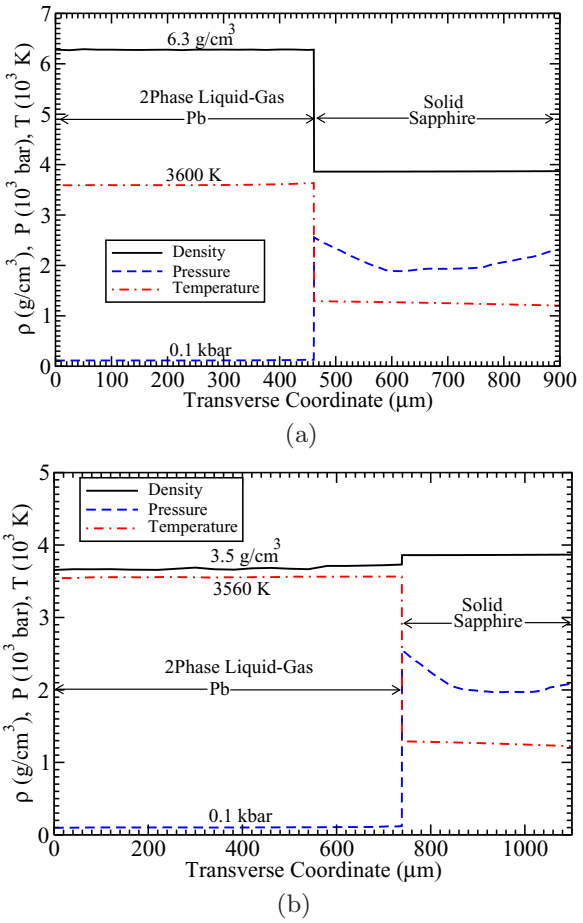

FIG. 11. Same as in Fig. 10 but using FWHM $= 3$ mm; (a) at $t = 500$ ns and (b) at $t = 1000$ ns.

2. *One-dimensional profiles using FWHM of 3 mm*

The results obtained using FWHM $= 3$ mm are presented in this section. The simulations show that a specific energy of 0.78 kJ/g is deposited in the lead sample, while a higher value of 1.12 kJ/g is generated in the sapphire. In Figs. 11(a) and 11(b), we present the profiles of the physical parameters at $t =$ 500 ns and 1000 ns, respectively. It is seen in Fig. 11(a) that the lead density is 6.3 g/cm^3, the temperature is about 3600 K, while the pressure is around 0.1 kbar and the material is in two-phase liquid-gas state. The temperature in the sapphire is of the order of 1200 K, which means that the sapphire plates remain solid.

Figure 11(b) shows that the lead density has been reduced to 3.5 g/cm^3 due to further expansion, and the material is still in two-phase liquid-gas state. It is also to be noted that the profiles are very uniform in the lead region. We also note that during the earlier times, first the material is transformed into a liquid and then enters the two-phase region. However, we only present a few selected profiles in the two-phase, liquid-gas region.

3. *One-dimensional profiles using FWHM of 2 mm*

We also carried out simulations using a FWHM of 2 mm and the results are summarized in the following.

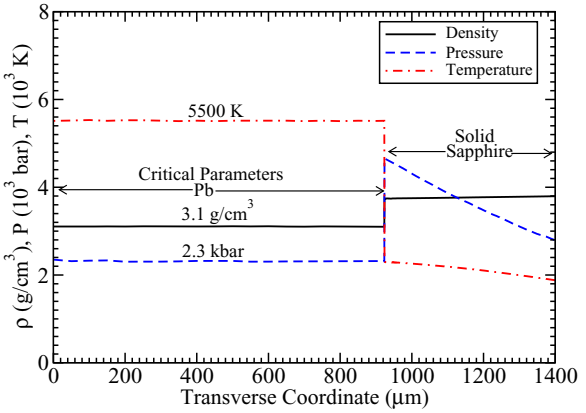

FIG. 12. Same as in Fig. 10 but using FWHM = 2 mm at t = 780 ns.

Since the focal spot size is small, the specific energy deposition is higher compared to the previous two cases. Simulations show that at $t = 100$ ns, when the bunch has just delivered its total energy, the specific energy deposition in the Pb is about 1.7 kJ/g that leads to a temperature of around 11 000 K and a pressure of about 20 GPa. The solid lead sample is converted into a high-density hot liquid. The sample expands due to the high pressure and the two sapphire plates are symmetrically pushed in the opposite direction along the transverse coordinate. The material density, temperature, and pressure continuously decrease due to expansion. In Fig. 12 we present the density, temperature, and the pressure profiles vs the transverse coordinate at $t = 780$ ns. It is seen that one achieves the lead critical parameters according to Table I. The simulations therefore predict that with the moderate beam intensity used in these calculations, it may be possible to access the lead critical parameters. Thus we conclude that using a beam intensity of 5×10^{10} and considering a suitable focal spot size, one can generate interesting HED phases of lead including liquid state, two-phase liquid-gas state, and critical parameter region.

The temperature in the sapphire is about 1900 K, which is still below its melting temperature which means that this configuration can still work with these beam parameters.

C. Bunch intensity 7.5×10^{10}

In this section we present a summary of the results obtained using an intensity of 7.5×10^{10} ions per bunch. Three different values of FWHM including 3.5, 3, and 2.5 mm, respectively, are considered. We note that we only provide a summary of the results and do not give the details to avoid repetition of the discussion presented in the previous sections.

1. One-dimensional profiles using FWHM of 3.5 mm

Simulations show that using a FWHM = 3.5 mm, the specific energy deposition in the lead part at $t = 100$ ns is 0.85 kJ/g, the temperature is about 6000 K, while the pressure is of the order of 12 GPa. The sample material is first converter into liquid and later enters two-phase liquid-gas state. In Fig. 13, we present the density, temperature, and the pressure vs transverse coordinate at $t = 480$ ns. It is seen that the material

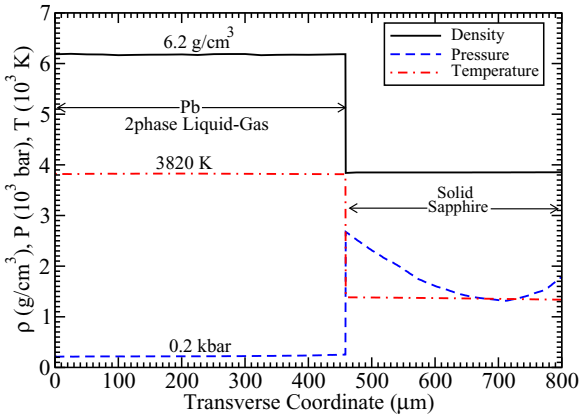

FIG. 13. Density (ρ), temperature (T), and pressure (P) vs transverse coordinate, intensity = 7.5×10^{10} uranium ions per bunch, particle energy = 1 GeV/u, bunch length = 100 ns, Gaussian transverse intensity distribution in focal spot with FWHM = 3.5 mm, sample thickness = 500 μm, sapphire thickness 500 μm (Fig. 3) at $t = 480$ ns.

is in two-phase liquid-gas state with a density of about 6 g/cm^3, a temperature of around 3800 K, and the pressure of the order of 0.2 kbar. This single time point is presented as an example, while different sets of the physical parameters in these two-phase region can be achieved at different times during the material expansion. It is also worth noting that the temperature in the sapphire is 1300 K, which is below its melting temperature.

2. One-dimensional profiles using FWHM of 3 mm

Using a FWHM of 3 mm, the simulations show that at t = 100 ns, a specific energy of 1.15 kJ/g is deposited in lead that generates a temperature of about 8000 K and a pressure of the order of 15 GPa and the material is converted into liquid state. As the material expands due to the high pressure, the density and the temperature are reduced and the material becomes a two-phase liquid-gas mixture. In Fig. 14 we present, as an example, the lead physical parameters at $t = 600$ ns, which shows a density of 4.7 g/cm^3, a temperature of 4550 K, and a pressure of 0.9 K. Different sets of parameters in the

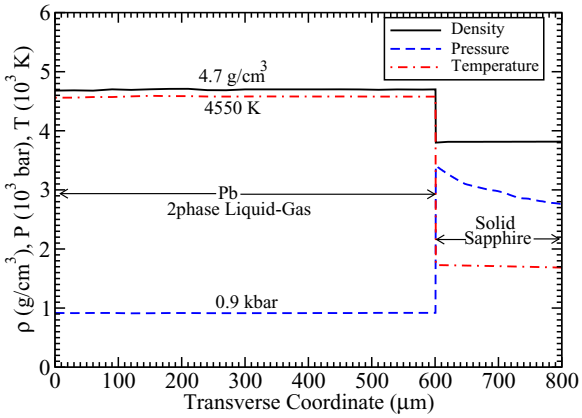

FIG. 14. Same as in Fig. 13 but using FWHM = 3 mm at t = 600 ns.

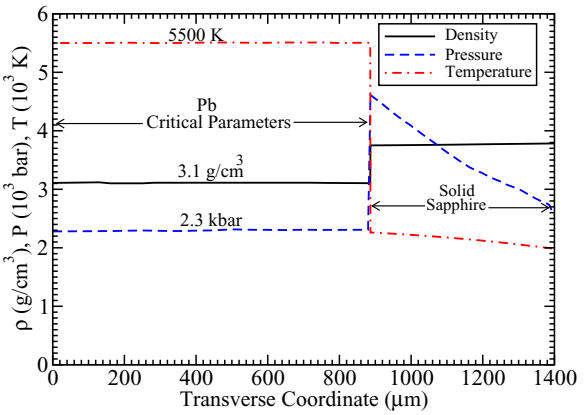

FIG. 15. Same as in Fig. 13 but using FWHM = 2.5 mm at t = 760 ns.

two-phase state can be accessed at different times during the target expansion. The sapphire temperature is of the order of 1700, which is safely below the melting temperature.

3. One-dimensional profiles using FWHM of 2.5 mm

According to our simulations, in this case, a specific energy deposition of about 1.7 kJ/g is deposited in lead at the end of the bunch (t = 100 ns). This leads to a temperature of around 11 000 K and a pressure of the order of 20 GPa. In Fig. 15 the profiles of the physical parameters at t = 760 ns are presented. It is interesting to note that with these beam parameters, one can access the critical parameters of lead. The sapphire temperature is of the order of 2100 K, which still is less than the melting temperature and this the window will still be solid during the measurements.

D. Summary of results

In Fig. 16 we present a 3D phase diagram of Pb in P-V-T space. The line marked with M represents the melting curve, whereas the label R represents the evaporation curve. Moreover, H_1 represents the principal Hugoniot, Hp shows the shock adiabat of porous lead, S represent various release isentropes, 1 denotes the IEX data for Pb, 2–18 denote data sets obtained in simulations, 19 is γ, the plasma nonideality parameter, and 20 denotes α, the ionization rate according to the chemical model of plasma with strong interaction between charged particles [95].

In order to predict the physical states that can be accessed in the proposed HIHEX experiments, we plot on this figure the data sets obtained in our simulations. It is seen that within the range of the beam parameters used in the simulations presented in this paper and the proposed target design, it is possible to access the liquid state, expanded hot liquid state, two-phase liquid-gas state, and the critical parameter region of lead.

In Table II we present a brief summary of the results showing the physical state that can be achieved using a given intensity and a specific focal spot size. It is seen that using a bunch intensity of 3×10^{10} ions/bunch and a FWHM of 2 mm, one first achieves a high-density hot liquid (at the end of the bunch), which then becomes an expanded hot liquid

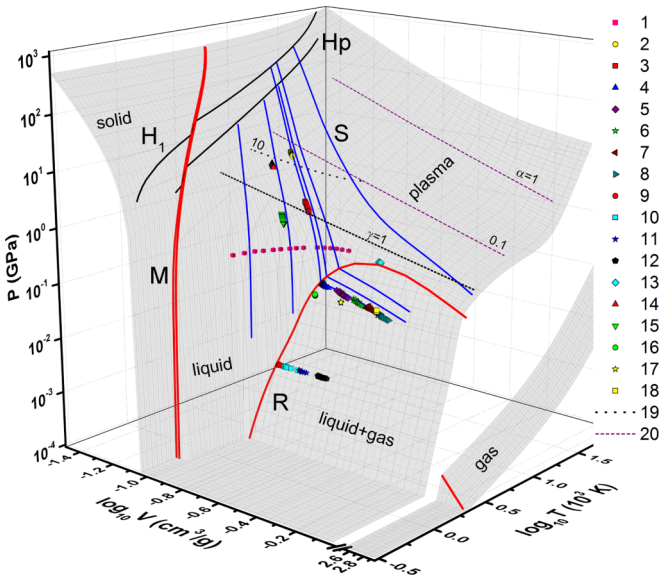

FIG. 16. Three-dimensional phase diagram of Pb in P-V-T space. The line marked with M represents the melting curve, the label R represents the evaporation curve, H_1 represents the principal Hugoniot, Hp shows the shock adiabat of porous lead, S represent various release isentropes, 1 denotes IEX data for Pb, 2–18 denote data sets obtained in simulations, 19 denotes γ, the plasma nonideality parameter, and 20 denotes α, the ionization rate according to the chemical model of plasma with strong interaction between charged particles [95].

due to the expansion of the material. At a later time when the density decreases further and the temperature is reduced, the material enters the two-phase liquid-gas regime. The same pattern is seen using a FWHM of 2.5 mm.

In the case of a bunch intensity of 5×10^{10} ions/bunch, using a FWHM of 2 mm, the specific energy is high enough to access the critical parameters after the material is liquefied and expansion takes place. However, using the larger values of the FWHM, only a two-phase liquid-gas state is finally achieved.

Using a bunch intensity of 7.5×10^{10} ions/bunch, one can generate the critical parameter conditions even with a FWHM of 2.5 mm, whereas with bigger vales of FWHM, a two-phase liquid-gas state can be achieved.

TABLE II. Sample physical state achieved considering different bunch intensities and different focal spot sizes using a uranium 1-GeV/u beam with bunch length 100 ns; HDL denotes high-density liquid, EHL denotes expanded hot liquid, 2PLG denotes two-phase liquid-gas mixture, and CP denotes critical parameters.

Bunch intensity	FWHM (mm)	Physical state
3×10^{10}	2	HDL/EHL/2PLG
	2.5	HDL/EHL/2PLG
5×10^{10}	2	HDL/EHL/CP
	3	HDL/EHL/2PL
	3.5	HDL/EHL/2PL
7.5×10^{10}	2.5	HDL/EHL/CP
	3	HDL/EHL/2PLG
	3.5	HDL/EHL/2PLG

VII. DIAGNOSTICS

The technique of heavy-ion heating and expansion can produce large and homogeneous samples at WDM conditions. These are ideally suited to perform accurate measurements of the sample state and its microscopic properties, which will allow stringent tests of dense matter theory or benchmarking of wide-range EOS models. In the experimental configuration discussed in this paper, the sample is in the solid or liquid phase and has a well-defined interface with a solid window transparent to optical radiation. This provides access to optical diagnostic techniques that are commonly used in shock physics experiments. For example, pyrometric measurements can be used to determine the surface temperature. For the predicted temperatures of 5000 to 10 000 K the maximum of the blackbody emission spectrum is in the optical regime at wavelengths between 600 and 300 nm. The spectral radiance strongly increases with the sample temperature and measuring the sample emission will yield the surface brightness temperature [96]. At a radiant emittance of several 100 W/mm^2, use of fast gated or streak cameras with a temporal resolution of 10 ns should be possible. Determining the slope of the spectral radiance, for example with simultaneous measurements at different wavelengths can alternatively yield a sensitive measurement of the color temperature [97]. Laser interferometric techniques will allow to measure the movement of the sample-window interface with high accuracy (for example, Ref. [98]). For a 1D-like expansion, this will directly provide the sample volume and thus the density. The assumption of a 1D expansion can be verified with space-resolved interferometric measurements [99,100]. Comparing the measured interface velocity with hydrodynamic simulations, and given the mechanical and optical response of the window material, the sample pressure can be inferred (for example, Ref. [101]). The measurement of sample volume, temperature, and pressure then yields a location on the equation-of-state surface. Finally, measurements of the sample reflectivity provide optical properties, which allows us, for example, to detect a metal to nonmetal transition [101].

Intense pulses of hard x-rays will enable diagnostic techniques probing volumetric properties. Such powerful x-ray sources can, for example, be generated by focusing high-energy laser pulses to intensities of the order of 10^{15} W/cm^2 onto mid-Z metal targets producing a hot plasma emitting resonance line radiation of highly charged ions [102], with μm high efficiency reaching photon energies up to 10 keV. The attenuation length for photons at 10 keV in lead at liquid or solid density is approximately 7 μm and even several hundred in the window material. As long as the sample still is in the solid phase, the lattice temperature can be inferred from the diffracted intensity [103], for example, of the lead Pb (111)-reflection (at around 25° for 10 keV radiation). This is also a sensitive diagnostic for the solid-liquid transition. In the liquid regime, angle-resolved elastic x-ray scattering gives access to the static ion-ion structure factor [104]. The position of the first correlation peak of the liquid structure factor is inversely proportional to the average ion-ion distance [105] (the Wigner-Seitz radius $a_{WS} = [3/(4\pi n_i)]^{1/3}$), providing a direct measurement of the ion (and mass) density. Provided that the sample is sufficiently thin, diagnostic methods based on x-ray transmission also become applicable. x-Ray radiography across the sample could visualize explosive boiling when the sample crosses the liquid-vapor coexistence line into a superheated state. x-Ray absorption spectroscopy (in Pb, for example, around the M5 edge at 2.5 keV) can measure edge shifts or show rebinding of atomic states as the sample density decreases.

VIII. CONCLUSIONS

This paper demonstrates that intense heavy-ion beams have the potential to generate large samples of HED matter with fairly uniform physical conditions. It is emphasized that an ion beam driver can be used for this purpose employing two very different techniques. One scheme uses shock compression of matter, while the other considers isochoric and uniform heating of solid targets to achieve this goal. The former technique is suitable to generate a low-entropy compression that produces planetary core conditions. The latter, on the other hand, induces high-entropy states in the sample, which can be used to study the EOS properties and the phase transitions in the material.

Using detailed numerical simulations, we propose design of an experiment to be done using intense heavy-ion beam that will be generated at the FAIR facility. A multilayered target is used that is composed of a plate of the sample material (Pb in this case), which is sandwiched between two identical slabs of sapphire. The sapphire acts as an optical window for diagnosing the sample and, at the same time, it plays the role of a tamper that confines the sample for a longer time. We consider a uranium beam with a particle energy of 1 GeV/u, whereas the bunch length is 100 ns. Four different intensities, including 3×10^{10}, 5×10^{10}, 7.5×10^{10}, and 10^{11} ions per bunch, are considered. The transverse intensity distribution in the focal spot is assumed to be Gaussian. A wide range of focal spot size characterized with a FWHM in the range 1 to 3.5 mm is used. The simulations show that, using the above moderate beam intensities and a suitable focal spot size, one can generate interesting physical states of HED Pb, which include an expanded hot liquid state, a two-phase liquid-gas state, and the critical parameters. Similar studies are planned for other metals.

ACKNOWLEDGMENT

This work was financially supported by the Bundesministerium für Bildung und Forschung (BMBF).

[1] R. P. Drake, Phys. Plasmas **16**, 055501 (2009).

[2] V. E. Fortov, *Extreme States of Matter* (Springer-Verlag, Heidelberg, 2016).

[3] D. Mihalas, *Stellar Atmospheres* (W. H. Freeman & Co., San Francisco, 1978).

[4] M. Zeilik and S. A. Gregory, *Introduction to Astronomy and Astrophysics* (Saunders College Publishing, Philadelphia, PA, 1998).

[5] E. J. Rivera, J. J. Lissauer, R. P. Butler *et al.*, Astrophys. J. Suppl. Ser. **634**, 625 (2005).

[6] D. Valencia, D. D. Sasselov, and R. J. O'Connel, Astrophys. J. Suppl. Ser. **665**, 1413 (2007).
[7] C. Sotin, O. Grasset, and A. Mocquet, Icarus **191**, 337 (2007).
[8] D. C. Swift, J. G. Eggert, D. G. Hicks *et al.*, Astrophys. J. **744**, 59 (2012).
[9] J. Nuckolls, L. Wood, A. Thiessen *et al.*, Nature **239**, 139 (1972).
[10] K. A. Brueckner and S. Jorna, Rev. Mod. Phys. **46**, 325 (1974).
[11] J. D. Lindl, Phy. Plasmas **2**, 3933 (1995).
[12] S. Ichimaro, *Strongly Coupled Plasma Physics* (Elsevier, Amsterdam, 1990).
[13] V. E. Fortov, I. T. Iakubov, and A. G. Khrapak, *Physics of Strongly Coupled Plasmas* (Clarendon Press, Oxford, 2006).
[14] M. Murillo, Phys. Plasmas **11**, 2964 (2004).
[15] H. K. Mao and R. J. Hemley, Rev. Mod. Phys. **66**, 671 (1994).
[16] C. Narayan, H. Luo, and A. L. Ruoff, Nature **393**, 46 (1998).
[17] R. G. McQueen, S. P. Marsh, J. W. Taylor, and J. N. Fritz, in *High Velocity Impact Phenomena*, edited by R. Kinslow (Academic, New York, 1970), pp. 293–417.
[18] L. V. Altshuler, Sov. Phys. Usp. **8**, 52 (1965).
[19] Ya. B. Zeldovich and Yu. P. Raizer, *Physics of Shock Waves and High temperature Phenomenon* (Academic, New York, 1966).
[20] *Compendium of Shock Wave Data*, edited by M. van Thiel, Lawrence Livermore Laboratory Report No. UCRL-50108, (1977).
[21] *LASL Shock Hugoniot Data*, edited by S. P. Marsh (University of California Press, Berkeley, 1980).
[22] M. V. Zhernokletov, V. N. Zubarev, R. F. Trunin, and V. E. Fortov, *Experimental Data on Shock Compression and Adiabatic Expansion of Condensed Materials at High Energy Density* (IPCP RAS, Chernogolova, 1966). [in Russian]
[23] M. D. Knudson, D. L. Hanson, J. E. Bailey, C. A. Hall, J. R. Asay, and W. W. Anderson, Phys. Rev. Lett. **87**, 225501 (2001).
[24] A. S. Vladimirov, N. P. Voloshin, V. N. Nogin, A. V. Petrovtsev, and V. A. Siminenko, JETP Lett. **39**, 82 (1984).
[25] T. Löwer, R. Sigel, K. Eidmann, I. B. Földes, S. Hüller, J. Massen, G. D. Tsakiris, S. Witkowski, W. Preuss, H. Nishimura, H. Shiraga, Y. Kato, S. Nakai, and T. Endo, Phys. Rev. Lett. **72**, 3186 (1994).
[26] R. Cauble, D. W. Phillion, T. J. Hoover, N. C. Holmes, J. D. Kilkenny, and R. W. Lee, Phys. Rev. Lett. **70**, 2102 (1993).
[27] M. Koenig, B. Faral, J. M. Boudenne, D. Batani, A. Benuzzi, S. Bossi, C. Rémond, J. P. Perrine, M. Temporal, and S. Atzeni, Phys. Rev. Lett. **74**, 2260 (1995).
[28] D. Batani, A. Balducci, D. Beretta, A. Bernardinello, T. Löwer, M. Koenig, A. Benuzzi, B. Faral, and T. Hall, Phys. Rev. B **61**, 9287 (2000).
[29] W. F. Henning, Nucl. Instrum. Methods B **214**, 211 (2004).
[30] D. Krämer, in *Proceeedings of the 10th European Particle Acceleration Conference (EPAC'06), Edinburgh, UK, June 26–30, 2006*, edited by C. Prior (CERN, Geneva, 2006), http://www.epac06.org.
[31] P. J. Spiller, M. Bai, D. Boine Frankenheim *et al.*, in *Proceedings of the 9th International Particle Acceleration Conference (IPAC18), Vancover, Canada, April 29–May 4, 2018*, Journal of Physics: Conference Series (2018), p. 1067.
[32] M. Durante, P. Indelicato, B. Johnson *et al.*, Phys. Scr. **94**, 033001 (2019).
[33] U. N. Funk, R. Bock, M. Dornik *et al.*, Nucl. Instrum. Methods A **415**, 68 (1998).
[34] N. A. Tahir, D. H. H. Hoffmann, J. A. Maruhn *et al.*, Phys. Plasmas **5**, 4426 (1998).
[35] N. A. Tahir, A. Kozyreva, P. Spiller, D. H. H. Hoffmann, and A. Shutov, Phys. Rev. E **63**, 036407 (2001).
[36] N. A. Tahir, A. Shutov, D. Varentsov *et al.*, Phys. Rev. Spec. Top.-Accel. Beams **6**, 020101 (2003).
[37] N. A. Tahir, A. Shutov, I. V. Lomonosov *et al.*, High Energy Density Phys. **2**, 21 (2006).
[38] N. A. Tahir, P. Spiller, S. Udrea *et al.*, Nucl. Instrum. Methods B **245**, 85 (2006).
[39] N. A. Tahir, Th. Stöhlker, A. Shutov *et al.*, New J. Phys. **12**, 073022 (2010).
[40] N. A. Tahir, A. Shutov, A. P. Zharkov *et al.*, Phys. Plasmas **18**, 032704 (2011).
[41] N. A. Tahir, I. V. Lomonosov, B. Borm *et al.*, Astrophys. J. Suppl. Series **232**, 1 (2017).
[42] N. A. Tahir, A. Shutov, I. V. Lomonosov *et al.*, Astrophys. J. Suppl. Series **238**, 27 (2018).
[43] N. A. Tahir, I. V. Lomonosov, B. Borm *et al.*, Contribu. Plasma Phys. **57**, 493 (2017).
[44] A. R. Piriz, J. J. Lopez Cela, M. C. Serna Moreno *et al.*, Laser Part. Beams **24**, 275 (2006).
[45] A. R. Piriz, J. J. López Cela, N. A. Tahir, and D. H. H. Hoffmann, Phys. Rev. E **74**, 037301 (2006).
[46] A. R. Piriz, Y. B. Sun, and N. A. Tahir, Phys. Rev. E **88**, 023026 (2013).
[47] A. R. Piriz, Y. B. Sun, and N. A. Tahir, Phys. Rev. E **89**, 063022 (2014).
[48] S. A. Piriz, A. R. Piriz, and N. A. Tahir, Phys. Fluids **30**, 111703 (2018).
[49] S. A. Piriz, A. R. Piriz, and N. A. Tahir, Phys. Rev. E **97**, 043106 (2018).
[50] S. A. Piriz, A. R. Piriz, and N. A. Tahir, J. Fluid Mech. **867**, 1012 (2019).
[51] M. Temporal, A. R. Piriz, N. Grandjouan *et al.*, Laser Part. Beams **21**, 609 (2003).
[52] H. Geissel, H. Weick, M. Winkler *et al.*, Nucl. Instrum. Methods B **204**, 71 (2003).
[53] M. Winkler, H. Geissel, H. Weick *et al.*, Nucl. Instrum. Methods B **266**, 4183 (2008).
[54] N. A. Tahir, V. Kim, A. Matveichev *et al.*, Laser Part. Beams **26**, 273 (2008).
[55] R. O. Bangerter, J.-W. K. Mark, and A. R. Thiesen, Phys. Lett. A **88**, 225 (1982).
[56] C. Deutsch, Ann. Phys. (Paris) **11**, 1 (1986).
[57] B. G. Logan, L. J. Perkins, and J. J. Bernard, Phys. Plasmas **15**, 072701 (2008).
[58] G. R. Magelssen, Nucl. Fusion **24**, 1527 (1984).
[59] A. R. Piriz, Phys. Fluids **31**, 658 (1988).
[60] N. A. Tahir and K. A. Long, Phys. Lett. A **90**, 242 (1982).
[61] N. A. Tahir and K. A. Long, Laser Part. Beams **2**, 371 (1983).
[62] N. A. Tahir and K. A. Long, Phys. Fluids **29**, 1282 (1986).
[63] N. A. Tahir and K. A. Long, Z. Phys. A **325**, 99 (1986).
[64] K. A. Long and N. A. Tahir, Phys. Lett. A **91**, 451 (1982).
[65] K. A. Long and N. A. Tahir, Nucl. Fusion **26**, 555 (1986).
[66] K. A. Long and N. A. Tahir, Phys. Rev. A **35**, 2631 (1987).

[67] N. A. Tahir, B. Goddard, V. Kain *et al.*, J. Appl. Phys. **97**, 083532 (2005).
[68] N. A. Tahir, R. Schmidt, A. Shutov, I. V. Lomonosov, A. R. Piriz, D. H. H. Hoffmann, C. Deutsch, and V. E. Fortov, Phys. Reve. E **79**, 046410 (2009).
[69] J. Neufeld, Phys. Rev. **95**, 1128 (1954).
[70] J. F. Ziegler, J. P. Biersack, and U. Littmark, *The Stopping and Ranges of Ions in Solids* (Pergamon Press, New York, 1996).
[71] P. Sigmund, *Particle Penetration and Radiation Effects* (Springer-Verlag, Berlin, 2006).
[72] A. Meftah, H. Behacine, A. Benyagoub *et al.*, Nucl. Instrum. Methods B **366**, 155 (2016).
[73] P. Mota-Santiago, H. Vazquez, T. Bierschenk *et al.*, Nanotechnology **29**, 144004 (2018).
[74] J. Habainy, K. Lee, K. B. Surreddi *et al.*, Nucl. Instrum. Methods B **439**, 7 (2019).
[75] R. A. Snavely, M. H. Key, S. P. Hatchett, T. E. Cowan, M. Roth, T. W. Phillips, M. A. Stoyer, E. A. Henry, T. C. Sangster, M. S. Singh, S. C. Wilks, A. MacKinnon, A. Offenberger, D. M. Pennington, K. Yasuike, A. B. Langdon, B. F. Lasinski, J. Johnson, M. D. Perry, and E. M. Campbell, Phys. Rev. Lett. **85**, 2945 (2000).
[76] M. Allen, P. K. Patel, A. Mackinnon, D. Price, S. Wilks, and E. Morse, Phys. Rev. Lett. **93**, 265004 (2004).
[77] A. Macchi, M. Borghesi, and M. Passoni, Rev. Mod. Phys. **85**, 751 (2013).
[78] F. Wagner, C. Brabetz, O. Deppert *et al.*, High Power Laser Eng. Sci. **4**, e45 (2016).
[79] D. Khaghani, M. Lobet, B. Borm *et al.*, Sci. Rep. **7**, 11366 (2017).
[80] P. Hiltz, T. M. Ostermayer, A. Huebel *et al.*, Nat. Commun. **9**, 423 (2018).
[81] P. K. Patel, A. J. Mackinnon, M. H. Key *et al.*, Phys. Rev. Lett. **91**, 125004 (2003).
[82] A. Soloviel, K. Burdonov, S. N. Chen *et al.*, Sci. Rep. **7**, 12144 (2017).
[83] G. R. Gathers, Rep. Prog. Phys. **49**, 341 (1986).
[84] V. K. Gryaznov, V. E. Fortov, M. V. Zhernokletov *et al.*, JETP **87**, 678 (1998).
[85] V. E. Fortov and I. T. Yakubov, *Physics of Nonideal Plasmas* (World Scientific, London, 1999).
[86] R. W. Ohse and H. von Tippelskirch, High Temp.- High Press. **9**, 367 (1977).
[87] V. E. Fortov, K. V. Khishchenko, P. R. Levashov *et al.*, Nucl. Instrum. Methods A **415**, 604 (1998).
[88] H. S. Bal, Characterization of Sapphire: Material Properties at High Temperatures, Ph.D. thesis, University of Florida (2015).
[89] S. K. Godunov, V. A. Zabrodin, M. L. Ivanov *et al.*, Nauka, Moscow (1976).
[90] V. E. Fortov, B. Goel, C. D. Munz *et al.*, Nucl. Sci. Eng. **123**, 169 (1996).
[91] I. V. Lomonosov, Laser Part. Beams **25**, 567 (2007).
[92] V. E. Fortov and I. V. Lomonosov, Phys. Usp. **57**, 219 (2014).
[93] J. J. Barnard, J. Armijo, R. M. More *et al.*, Nucl. Instrum. Methods A **577**, 275 (2007).
[94] A. S. Khan and S. Huang, *Continuous Theory of Plasticity* (J. Wiley & Sons, Inc., New York, 1995).
[95] I. V. Lomonosov and V. K. Gryaznov, Contrib. Plasma Phys. **56**, 302 (2016).
[96] J. H. Eggert, D. G. Hicks, P. M. Celliers *et al.*, Nat. Phys. **6**, 40 (2010).
[97] T. A. Hall, A. Benuzzi, D. Batani *et al.*, Phys. Rev. E **55**, R6356 (1997).
[98] V. N. Korobenko and A. D. Rakhel, J. Phys.: Condens. Matter **26**, 045701 (2014).
[99] P. M. Celliers, D. K. Bradley, G. W. Collins *et al.*, Rev. Sci. Instrum. **75**, 4916 (2004).
[100] P. M. Celliers, D. J. Erskine, C. M. Sorce *et al.*, Rev. Sci. Instrum. **81**, 035101 (2010).
[101] M. D. Knudson, M. P. Desjarlais, A. Becker *et al.*, Science **348**, 1455 (2015).
[102] R. E. Ruggles, J. L. Porter Jr., P. K. Rambo *et al.*, Rev. Sci. Instrum. **74**, 2206 (2003).
[103] T. G. White, J. Vorberger, C. R. D. Brown *et al.*, Sci. Rep. **2**, 889 (2012).
[104] L. B. Fletcher, H. J. Lee, T. Doppner *et al.*, Nat. Photon. **9**, 274 (2015).
[105] W. Schirmacher, *Theory of Liquids and Other Disorder Media* (Springer, Berlin, 2015).